Energy Storage Materials 69 (2024) 103421

Contents lists available at ScienceDirect

Energy Storage Materials

journal homepage: www.elsevier.com/locate/ensm

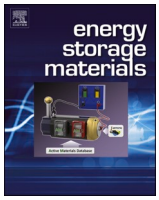

Millisecond activity modulation of atomically-dispersed Fe–N–C catalysts

Guobin Qin [a], Sida Sun [b], Xuehuan Zhang [a], Zhen Han [b], Yanping Li [a], Gaoyi Han [a,c], Yan Li [b,c], Sheng Zhu [a,c,d,*]

[a] Institute of Molecular Science, Key Laboratory of Materials for Energy Conversion and Storage of Shanxi Province, Key Laboratory of Chemical Biology and Molecular Engineering of Education Ministry, Shanxi University, Taiyuan 030006, China
[b] Beijing National Laboratory for Molecular Science, Key Laboratory for the Physics and Chemistry of Nanodevices, College of Chemistry and Molecular Engineering, Peking University, Beijing 100871, China
[c] Institute for Carbon-Based Thin Film Electronics, Peking University, Shanxi (ICTFE-PKU), Taiyuan 030012, China
[d] Institute of Advanced Functional Materials and Devices, Shanxi University, Taiyuan 030031, China

ARTICLE INFO

Keywords:
Fe–N–C catalyst
Oxygen reduction
Zinc-air battery
Flash Joule heating
Electrocatalysis

ABSTRACT

Precious-metal-free transition metal–N–C catalysts containing atomic MeN_x centers are promising candidates for the oxygen reduction reaction (ORR) in rechargeable zinc-air batteries. In this study, we report the highly efficient synthesis and activity modulation of Me–N–C (Me = Fe, Co, Ni, and Cu) catalysts utilizing the flash Joule heating technique, accomplished within 200 milliseconds. The instantaneous high temperature (~3535 K) and rapid heating and cooling rates (above 10^4 K s^{-1}) induce the formation of atomically-dispersed MeN_x sites on the surface of carbon nanotube matrices. This ultrafast thermal shock process not only prevents the aggregation of isolated metal atoms but also achieves catalytic activity modulation through heteroatom engineering. Typically, phosphorus atoms play a crucial role in suppressing nitrogen loss and regulating the local coordination environment of FeN_x centers, thereby facilitating the 4 e^- electrocatalytic reduction of oxygen. As expected, the phosphorus-doped Fe–N–C catalyst exhibits excellent ORR activity with a high half-wave potential of 0.904 V and a low Tafel slope of 23.1 mV dec^{-1} in a 0.1 M KOH medium. The assembled zinc-air battery demonstrates a prominent power density of 236.3 mW cm^{-2} and desirable long-term durability over 400 h, surpassing that of the Pt/C+IrO_2-based battery.

1. Introduction

Efficient and stable oxygen reduction catalysts play a crucial role in advancing the commercialization of rechargeable zinc-air batteries (ZABs) [1–6]. In recent years, single-atom catalysts comprising transition metals coordinated with nitrogen and carbon (Me–N–C, where Me = Fe, Co, Ni, Cu, Mn, Mo, etc.) have emerged as promising alternatives to state-of-the-art platinum-based catalysts [7–9]. These materials offer several advantages, including cost-effectiveness and maximized atom utilization [10–13]. Furthermore, they exhibit desirable catalytic activity for the oxygen reduction reaction (ORR) with excellent methanol tolerance [14–16]. Among them, atomically-dispersed Fe–N–C catalysts have garnered significant research interests [17,18]. In these catalysts, the FeN_x coordination serves as the active site for oxygen adsorption and ORR catalysis [19–22]. Currently, the majority of Fe–N–C catalysts are prepared using the traditional method of pyrolyzing iron, nitrogen, and carbon precursors [23–25]. However, this approach is time and energy-consuming, and it often leads to the aggregation of Fe atoms and nitrogen loss during prolonged heating, resulting in a reduced number of atomically dispersed FeN_x centers [26]. Therefore, the development of efficient synthesis techniques is of paramount importance to advance the investigation and application of Fe–N–C catalysts.

Recently, the flash Joule heating (FJH) technique has gained widespread recognition as a versatile method for synthesizing carbon nanomaterials [27–30]. In 2020, Tour and co-authors pioneered the use of FJH to achieve rapid and gram-scale production of turbostratic graphene [31]. Various inexpensive carbon sources, such as coal, biochar, carbon black, and plastic waste, can be rapidly converted into graphene with high purity and quality. Building on this breakthrough, our team successfully synthesized few-layer nitrogen-doped graphene within one second [32]. The prepared graphene with minimum structure defects were utilized as electrode material for high-rate energy storage devices. The FJH process stands out for its solvent-free, inert gas-free, etchant--free, and template-free attributes [33]. Remarkably, the extremely high

* Corresponding author.
E-mail address: shengzhu@sxu.edu.cn (S. Zhu).

https://doi.org/10.1016/j.ensm.2024.103421
Received 22 December 2023; Received in revised form 19 April 2024; Accepted 19 April 2024
Available online 27 April 2024

heating temperatures (> 3000 K) and ultrafast heating and cooling rates (> 10^4 K s^{-1}) are particularly advantageous for preparing atomically-dispersed Me–N–C catalysts [34]. For instance, Xi and colleagues achieved precise control over the monoatomic structure when synthesizing Ni–N–C catalysts. In this configuration, 80 % of the doped nitrogen atoms formed NiN_4 active sites [35]. The resulting catalyst demonstrated a high Faradaic efficiency for CO_2 reduction to CO across a wide applied voltage range (–0.7 to –1.9 V vs. RHE). Previous studies that attempted to synthesize Me–N–C materials using the Joule heating method fell short of achieving ideal ORR catalysts. The main challenge is that at high heating temperatures, outer nitrogen species tend to escape, resulting in a lower concentration of MeN_x sites on the surface of the carbon matrices and, consequently, poor catalytic performance [36]. Therefore, there is an urgent need to simultaneously achieve rapid production and activity modulation of Me–N–C catalysts during the FJH process to obtain efficient ORR catalysts, although this remains a formidable challenge.

In this study, we showcase the millisecond synthesis of atomically-dispersed Me–N–C as highly efficient ORR electrocatalysts. The catalytic activity is modulated by heteroatom engineering during ultrafast Joule heating process within 200 ms. Our findings reveal that the introduction of P dopants significantly enhances the ORR performance. This enhancement is attributed to their ability to restrain nitrogen loss and alter local coordination environment of the MeN_4 centers, resulting in a decreased energy barrier for the rate-determining step. This is supported by density functional theory (DFT) calculations. Impressively, the P-doped Fe–N–C catalyst exhibits a prime half-wave potential and a low Tafel slope under alkaline conditions, surpassing that of Pt/C catalyst. Moreover, the assembled ZABs exhibit high power density, excellent charge-discharge ability, and long-term durability.

2. Experimental section

2.1. Synthesis of FePC-CNT precursor

Firstly, 100 mg of multi-walled carbon nanotubes (MWCNTs) and 150 mg of FePc were separately dispersed in 120 mL and 60 mL of DMF solutions, respectively. The suspensions were subjected to ultrasonication for 0.5 h. Subsequently, the FePc dispersions were carefully combined with the MWCNT solution and subjected to ultrasonication for an additional hour. Finally, the mixed suspensions were collected after stirring for 24 h, which were then washed with ethanol and deionized water, followed by drying in a vacuum oven at 80 °C for 8 h to obtain the FePc-CNTs.

2.2. Synthesis of P-FeN_4@CNTs by FJH method

100 mg of FePc-CNTs and 50 mg of $NaH_2PO_2{\cdot}H_2O$ were thoroughly ground and placed into a quartz tube with a diameter of 10.0 mm. Conductive graphite plugs were positioned at both ends of the sample powders. Subsequently, the quartz tube was securely affixed to the reaction frame, and the sample's resistance was adjusted to a range of 1.0 to 2.0 Ω. The entire setup was then placed in a vacuum environment, and the flash voltage was set to 130 V. Throughout the reaction, temperature and current-versus-time curves were continuously recorded. The product yield is about 60 % and it is able to achieve gram-level production of catalyst by increasing the diameter of the quartz tube. For comparison, FeN_4@CNT was prepared under similar conditions but without the addition of $NaH_2PO_2{\cdot}H_2O$. To investigate the influence of different metal phthalocyanines on the ORR performance of the catalysts, P-CoN_4@CNTs, P-NiN_4@CNTs, and P-CuN_4@CNTs were also synthesized using the same procedure as that of the P-FeN_4@CNT catalyst. Other experimental details can be found in Supporting Information file.

3. Results and discussion

3.1. Synthesis and characterization

The schematic diagram of the synthetic route for P-MeN_4@CNTs is depicted in Fig. 1. Initially, various metal phthalocyanines (MePcs), including FePc, CoPc, NiPc, and CuPc, are immobilized on the outer surface of multi-walled carbon nanotubes (MWCNTs) *via* π–π interactions. Subsequently, the $NaH_2PO_2{\cdot}H_2O$ is added to the aforementioned mixtures, which will release PH_3 during heating process and incorporating phosphorus into the carbon framework [37]. The FJH method enables the ultrafast transformation of these feedstocks into atomically-dispersed P-MeN_x moieties on the surface of CNTs in less than 200 milliseconds (Video S1). During the reaction, the variations in reaction parameters are real-time recorded. From these recordings, we observe that the peak temperature and current are approximately 3535 K and 333 A, respectively.

Fig. S1 depicts the scanning electron microscopy (SEM) image of the P-FeN_4@CNT catalyst, demonstrating a uniform 1D structure without obvious agglomeration. To examine the form of Fe within this catalyst, aberration-corrected high-angle annular dark-field scanning transmission electron microscopy (AC—HAADF-STEM) images were collected and are shown in Fig. 2a. In these images, numerous individual bright dots (highlighted by red circles) correspond to atomically-dispersed Fe atoms, as seen in Fig. 2b. As further evidence, energy-dispersive X-ray spectroscopy (EDS) elemental mapping images show that C, N, Fe and P elements are uniformly distributed in the entire structure (Fig. S2). Fig. S3 provides the XRD patterns of P-FeN_4@CNTs prepared at different flash voltages. Two distinctive characteristic peaks, centered at 2θ angles of 25.7° and 43.1°, correspond to the (002) and (101) crystal planes of graphitic carbon [38]. Notably, no distinctive diffraction peaks associated with iron particles, iron oxides, or carbides are observed. The catalyst contains 1.487 wt.% of Fe and 0.589 wt.% of P, as determined by inductively coupled plasma-optical emission spectroscopy (Table S1).

In Raman spectroscopy (Fig. S4a), two distinct characteristic peaks at approximately 1345 cm^{-1} and 1582 cm^{-1} are attributed to the D and G bands, respectively. The relative intensity ratio between the D- and G-bands is commonly used to assess the structural defects of carbon materials [39,40]. As the FJH voltage increases, the I_D/I_G ratios of P-FeN_4@CNTs decrease from 1.28 to 0.99 (Fig. S4b), indicating that higher flash voltage contributes to the reduction of defect sites. The N_2 adsorption/desorption isotherms of P-FeN_4@CNTs exhibit typical type IV isotherms (Fig. S5a) [41], and the Brunauer-Emmett-Teller (BET) surface area of the P-FeN_4@CNT catalyst measures 91.4 m^2 g^{-1}. The pore size distribution curve in Fig. S5b reveals that the P-FeN_4@CNTs catalyst possesses a rich mesoporous structure within the range of 2 − 5 nm. Fig. S6 displays the X-ray photoelectron spectroscopy (XPS) spectra of P-FeN_4@CNTs prepared at different flash voltages. In all samples, three signal peaks for C 1 s, N 1 s, and O 1 s are observed. The C 1 s XPS profiles, as shown in Fig. S7a, are deconvoluted into three peaks at approximately 284.8 eV (C=C), 285.4 eV (C–N), and 287.5 eV (O–C=O) [42]. Furthermore, high-resolution N 1 s spectra at different voltages are provided in Fig. S7b. The peaks at 398.6 eV, 400.1 eV, and 404.1 eV are assigned to pyridinic-N and Fe–N_x, pyrrolic-N, and oxidized-N, respectively [43]. The Fe 2p and P 2p spectra (Fig. S8) of the typical P-FeN_4@CNTs confirm the successful doping of Fe and P after the instantaneous Joule heating process [44,45]. Importantly, P dopants effectively prevent nitrogen loss during the high-temperature heating process. The nitrogen content in P-FeN_4@CNTs is determined to be 3.64 at.%, over three times that of FeN_4@CNTs (1.16 at.%). The higher nitrogen content is favorable for creating more FeN_x active sites, which enhances ORR performance. Fig. S9 presents the infrared spectra of different P-FeN_4@CNTs [46,47].

The electronic structure and local coordination environment of the P-FeN_4@CNTs catalyst were investigated using X-ray absorption near edge

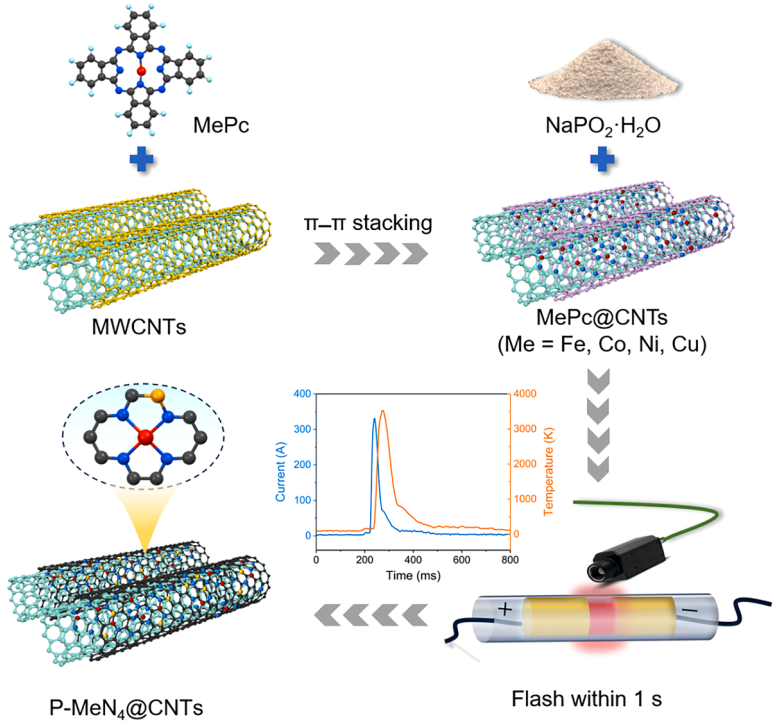

Fig. 1. Schematic diagram showing the synthesis process of atomically-dispersed catalysts of P-MeN_4@CNTs (Me = Fe, Co, Ni, and Cu).

structure (XANES) and extended X-ray absorption fine structure (EXAFS) measurements. For comparison, control samples including Fe foil, Fe_2O_3, FeP, and iron phthalocyanine (FePc) were employed. As shown in Fig. 2c, the XANES curves reveal that the absorption edge of P-FeN_4@CNTs falls between that of Fe foil and Fe_2O_3. This suggests that the valence state of the Fe atom in P-FeN_4@CNTs ranges between 0 and +2. Fig. 2d displays the k^3-weighted Fourier transform EXAFS curve of P-FeN_4@CNTs in R-space, where a prominent peak at approximately 1.5 Å is observed, corresponding to the Fe–N coordination. Importantly, no discernible signals for Fe−Fe or Fe−P coordination are detected.

To further investigate the coordination environment of Fe centers in *R* and *K* spaces, we employed wavelet-transformed (WT) EXAFS plots (Fig. 2e). Notably, the WT graph of P-FeN_4@CNTs exhibits a maximum strength at ~5.2 $Å^{-1}$ (Fe−N), which differs from the characteristics of Fe foil (~8.1 $Å^{-1}$) and Fe_2O_3 (~7.7 $Å^{-1}$). The local geometry of Fe in P-FeN_4@CNTs was analyzed using least-square EXAFS fitting (Fig. 2f and Table S2). The fitting curves in both R and K spaces align well with the experimental results. Simultaneously, the EXAFS fittings of the potential configurations containing two neighboring Fe atoms are shown in Fig. S11, S12, from which we observe the signal of Fe−Fe bond at ~2.20 Å, providing further evidence that iron atoms exist in the atomically-dispersed form. These findings strongly support the conclusion that Fe in P-FeN_4@CNTs exists in an atomically dispersed form, coordinated with four pyridinic-N atoms to form FeN_4 active sites [48]. Additionally, the presence of P atoms does not directly bind to the Fe atoms in the center of the first coordination shell; instead, they modulate the local structure by binding to adjacent N atoms.

3.2. ORR performance

The electrocatalytic ORR performances of P-FeN_4@CNTs were evaluated in O_2-saturated 0.1 M KOH solution. As can be seen from cyclic voltammetry (CV) and linear scanning voltammetry (LSV) profiles in Fig. S13 and Fig. 3a, the P-FeN_4@CNTs catalyst displays excellent ORR performance with a half-wave potential ($E_{1/2}$) of 0.904 V, higher than FePc-CNTs (0.866 V), FeN_4@CNTs (0.867 V), and 20 wt.% Pt/C (0.840 V). Fig. S14 shows LSV curves of P-FeN_4@CNTs at different rotating speeds from 400 to 2500 rpm, where the current densities present a positive correlation with the increase of rotational speeds. According to the K-L equation, the electron transfer numbers (n) of P-FeN_4@CNTs and 20 wt.% Pt/C are calculated to be 4.06 and 3.80, respectively (Fig. S15). It is proved that P-FeN_4@CNTs undergo a typical 4 e^- transfer pathway during ORR procedure. As shown in Fig. 3b, the Tafel slope of P-FeN_4@CNTs is 23.1 mV dec^{-1}, lower than that of FePc-CNTs (37.7 mV dec^{-1}), FeN_4@CNTs (25.5 mV dec^{-1}), and 20 wt.% Pt/C (59.4 mV dec^{-1}), implying its fast reaction kinetics [49,50]. This conclusion is confirmed by the electrochemical impedance spectroscopy (EIS) plots in Fig. S16a, in which the P-FeN_4@CNT catalyst has the smallest semicircle in the high frequency region and the most vertical line in the low frequency region [27,51]. Additionally, it exhibits a lower relaxation constant (τ) value of 1.45 s at −45° than Pt/C (23.81 s) in Bode diagram (Fig. S16b). Fig. 3c compares the $E_{1/2}$ and kinetics current density (j_K) of different samples. The j_K of P-FeN_4@CNTs reaches 33.48 mA cm^{-2} at −0.05 V, this value is almost 3.84, 2.92, and 6.39 times of FePc-CNTs (8.71 mA cm^{-2}), FeN_4@CNTs (11.45 mA cm^{-2}), and 20 wt.% Pt/C (5.24 mA cm^{-2}), respectively. Further, we analyzed the electrochemically-active surface area of these samples by calculating their specific double-layer capacitance (C_{dl}) at the non-Faraday regions (Fig. S17, S18), P-FeN_4@CNTs exhibit a large C_{dl} value of 6.54 mF cm^{-2}, accounting for its desirable capacitive property and catalytic activity. As depicted in Fig. 3d, the H_2O_2 yield and n of P-FeN_4@CNTs are further estimated through the rotating ring-disk electrode (RRDE). The H_2O_2 yield remains below 5 % and the electron transfer number close to four, which are consistent with the above analyses.

To optimize the ORR activity of P-FeN_4@CNTs, we varied the mass ratios of CNTs to FePc and $NaPO_2·H_2O$, ultimately determining them to be 1:1.5 and 2:1, respectively (Fig. S19, S20). Additionally, the effects of flash voltages on catalytic performance were explored, as shown in Fig. S21 and detailed in Table S3. The $E_{1/2}$ values corresponding to voltages of 90, 110, 130, 150, and 170 V were measured at 0.852, 0.886, 0.904, 0.845, and 0.837 V, respectively. The possible reasons are discussed for the superior ORR activity of P-FeN_4@CNTs when flashed at 130 V. Low voltages below 130 V with lower heating temperature would induce insufficient carbonization and thereby the poor graphitization

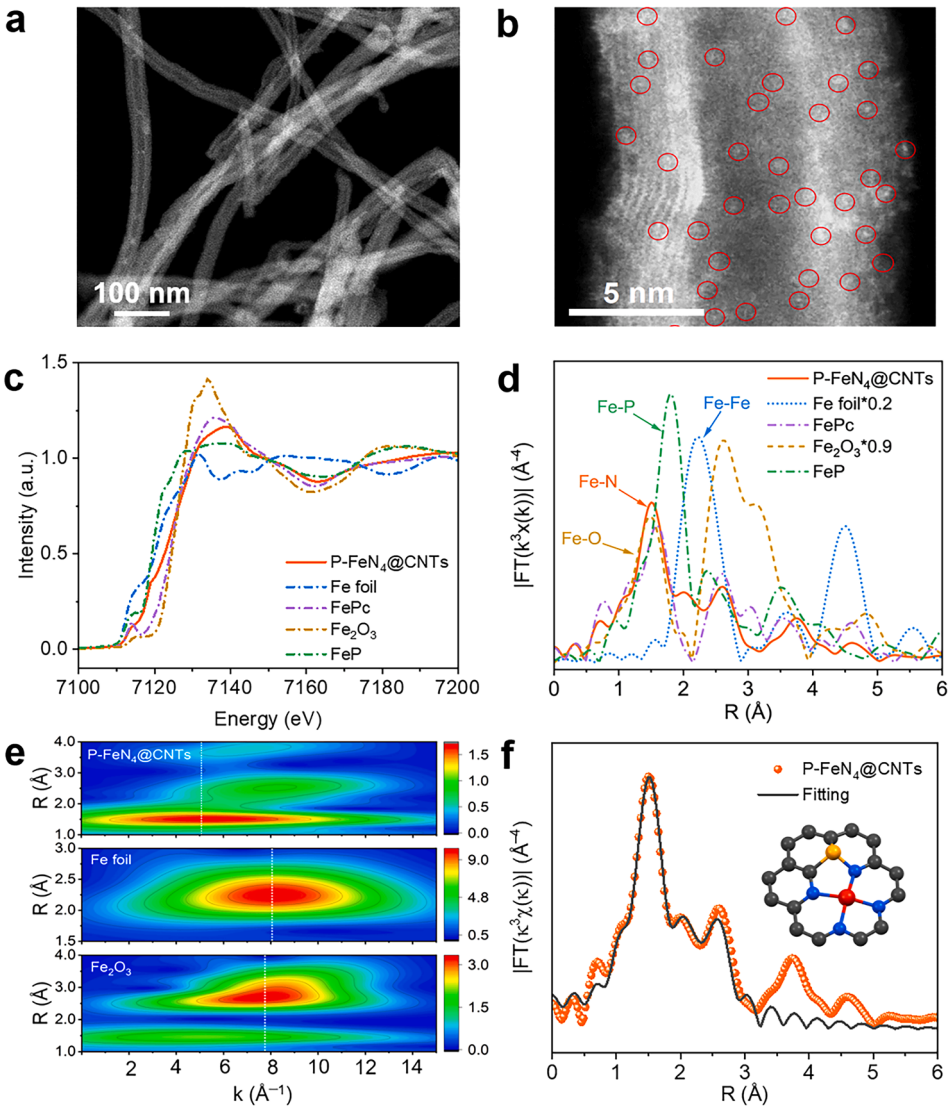

Fig. 2. Compositional and structural analysis of P-FeN_4@CNTs. (a, b) AC—HAADF STEM image of P-FeN_4@CNTs; (c) Fe K-edge XANES spectra of P-FeN_4@CNTs, FePc, Fe_2O_3, FeP, and Fe foil references; (d) k^3-weighted Fourier-transformed EXAFS spectra of P-FeN_4@CNTs, FePc, Fe_2O_3, FeP, and Fe foil; (e) k^3-weighted wavelet-transformed Fe K edge EXAFS spectra of P-FeN_4@CNTs, Fe_2O_3, and Fe foil; (f) EXAFS fitting curve of P-FeN_4@CNTs.

degree. Conversely, excessively high voltage-induced temperatures may cause partial loss of N and Fe, thereby reducing the number of available FeN_x active sites. Methanol-tolerant and stability performances of P-FeN_4@CNTs are estimated and compared with 20 wt.% Pt/C catalyst. The methanol-tolerant test was conducted in an O_2-saturated 0.1 M KOH electrolyte, injected with 2 M methanol solution at 200 s (Fig. 3e). It can be observed that the 20 wt.% Pt/C demonstrates a conspicuous change in current density, whereas P-FeN_4@CNTs display superior methanol-tolerant behavior with almost no fluctuation in j-t curve. The P-FeN_4@CNT catalyst presents a high current retention of about 96.69 % after 10 h, while Pt/C experiences a significant current decrease (~14.08%) under the same conditions (Fig. 3f), evidencing the remarkable long-term durability of the prepared flash catalyst. Moreover, the ORR catalytic performances of the P-FeN_4@CNTs are compared with the reported similar catalysts, as shown in Table S4. Impressively, the superior E_{ONSET}, $E_{1/2}$ and low Tafel slope values of P-FeN_4@CNT indicate its great potential as efficient ORR electrocatalyst. The OER performance of the catalysts was also investigated. As shown in Fig. S22a, the overpotential of the P-FeN_4@CNT catalyst is 443.4 mV at 10 mA cm^{-2}, which is close to RuO_2 (411.9 mV). It demonstrates desirable ability with 94.19 % current retention after 7 h (Fig. S22b). After testing, the structure of P-FeN_4@CNT catalyst is well maintained (Fig. S23).

3.3. Theoretical analyses

DFT calculations were performed to understand the effects of P atom in altering the coordination environment and ORR activity of the FeN_4 centers. Fig. 4a depicts four Fe−N−C configurations, where P bonds with N(1) and forms six and five membered rings in FeN_4P-1 and FeN_4P-2, respectively. As for FeN_4P-3, P locates at the para-position of Fe center in a six membered ring. The doping of P atom with large atomic radius induces tensile strain and local structure distortions of Fe−N−C, which depend upon the position of P-dopant. As shown in Fig. 4b, the FeN_4 center in undoped Fe−N−C presents a square-planar configuration with the Fe–N length of about 1.895 Å. This value undergoes distinctive variation after P doping, where the bond lengths of Fe–N(1), Fe–N(2), Fe–N(3) and Fe–N(4) in FeN_4P-2 configuration are 1.873 Å, 1.873 Å, 1.873 Å, and 1.951 Å, respectively. The four Fe–N bond lengths corresponding to FeN_4P-1 are 1.833 Å, 1.961 Å, 1.891 Å, 1.908 Å, while the bond lengths for FeN_4P-3 are 1.924 Å, 1.924 Å, 1.906 Å, 1.906 Å. Besides, the bond angles of three P-doped FeN_4 configurations also present

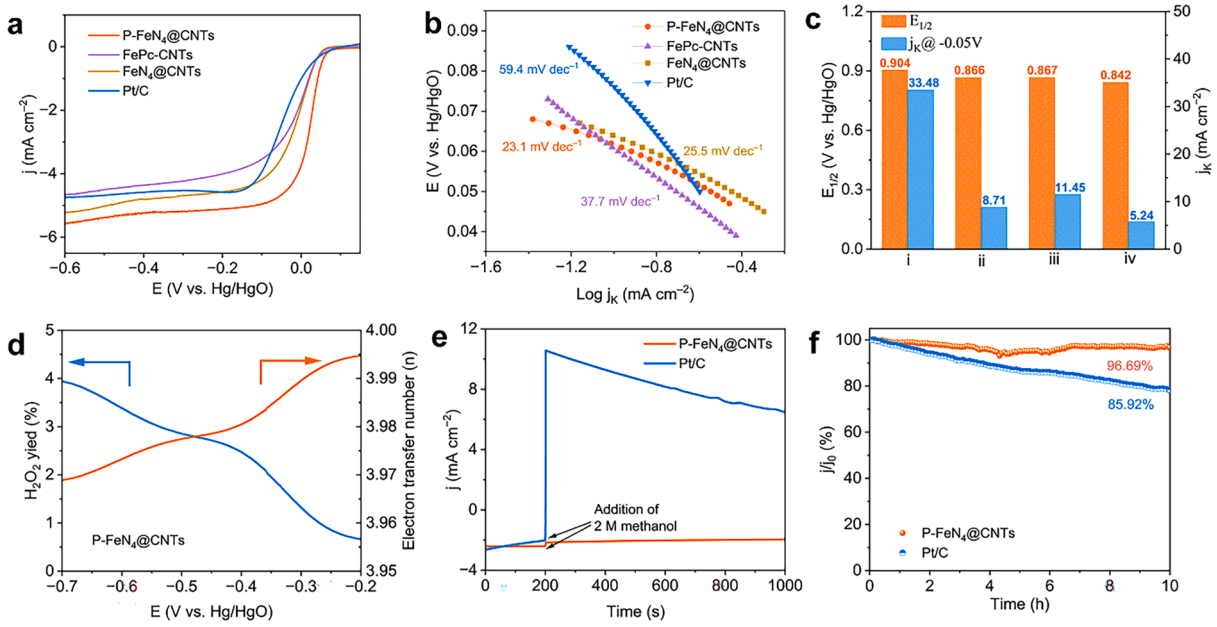

Fig. 3. Electrocatalytic ORR performances of P-FeN_4@CNTs. (a) ORR LSV curves of P-FeN_4@CNTs, FePc-CNTs, FeN_4@CNTs, and Pt/C electrocatalysts; (b) Tafel plots of P-FeN_4@CNTs, FePc-CNTs, FeN_4@CNTs, and Pt/C; (c) Histograms of $E_{1/2}$ and j_K of different samples. P-FeN_4@CNTs (i), FePc-CNTs (ii), FeN_4@CNTs (iii), and Pt/C (iv) electrocatalysts; (d) H_2O_2 yield of P-FeN_4@CNTs measured by RRDE; Methanol tolerance (e) and durability (f) performances of P-FeN_4@CNTs and Pt/C.

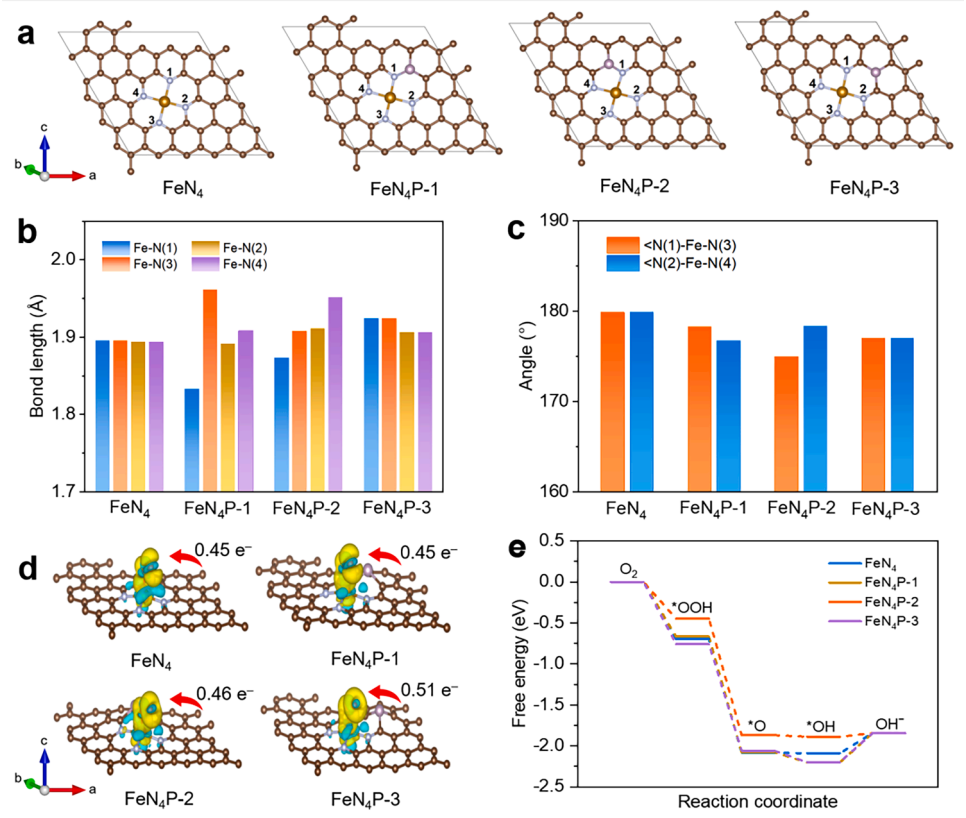

Fig. 4. DFT calculations of P-FeN_4@CNTs. (a) Optimized Fe–N–C and three representative P-doped Fe–N–C configurations. The balls in brown, grey, pink, and yellow colors represent C, N, P, and Fe atoms, respectively; Bar graphs of bond lengths (b) and bond angles (c) for Fe–N–C and three representative P-doped Fe–N–C models; (d) Charge density difference and Bader charge analysis of O_2 adsorbed on four Fe–N–C models; (e) Free energy diagrams for ORR process on four Fe–N–C models at 0 V vs RHE in the alkaline medium (pH = 13).

obvious changes compared to the raw FeN_4 (~180°), as displayed in Fig. 4c. Among them, FeN_4P-2 experiences the most pronounced symmetry distortion, with the N(1)–Fe–N(3) and N(2)–Fe–N(4) angles approaching 175.0° and 178.4°, respectively.

As mentioned previously, the presence of a P dopant significantly disrupts the planar symmetry of the FeN_4 configuration, leading to uneven charge distribution and subsequently influencing the adsorption and desorption behavior of oxygen intermediates [52,53]. As illustrated in Fig. 4d, P doping results in the donation of additional electrons to adsorbed O_2 species in FeN_4P-1 (0.45 e^-), FeN_4P-2 (0.46 e^-), and FeN_4P-3 (0.51 e^-), relative to pristine FeN_4 (0.45 e^-). Fig. 4e presents the free energy diagram for the four Fe–N–C catalysts, while Fig. S24–S27 depict the corresponding optimized structures of ORR intermediates (*OH, *O, and *OOH) on different FeN_4 configurations. All four configurations, including FeN_4 and the three FeN_4P configurations, exhibit the same rate-determining step of the *OH reduction ($*OH + e^- \rightarrow OH^- + *$). The FeN_4P-2 model shows an energy barrier of 0.045 eV for this step, this value is much lower than that of FeN_4 (0.244 eV), FeN_4P-1 (0.357 eV), and FeN_4P-3 (0.355 eV), indicating the lower ORR thermodynamic over-potential of FeN_4P-2 (Fig. S28 and Table S5). These analyses underscore that the position of doped P atom is highly related with the ORR performances of FeN_4 sites in atomically-dispersed Fe–N–C catalysts. On one hand, P doping can restrain the nitrogen loss during the ultrafast Joule heating process, leading to the formation of increased number of active FeN_4 sites. On the other hand, DFT results indicate that the presence of P dopant disrupts the planar symmetry of the FeN_4 configuration, resulting in uneven charge distribution and a reduced energy barrier for the rate-determining step, thereby enhancing the ORR performance.

3.4. Zinc-air batteries

To verify the versatility of the FJH technique in synthesizing the P-MeN_4@CNT catalysts, other common metal phthalocyanines including CoPc, NiPc, and CuPc are also employed as precursors. SEM images of P-CoN_4@CNT, P-NiN_4@CNT, and P-CuN_4@CNT catalysts all reveal uniform 1D tubular structure without significant agglomeration (Fig. S29–S31). Fig. S32 provides their corresponding XRD patterns, two distinct characteristic peaks centered at the 2θ degrees of 25.7° and 43.3° correspond to the (002) and (101) crystal planes of graphitic carbon, respectively. Importantly, no distinctive diffraction peaks of metal particles are observed, confirming the successful formation of atomically-dispersed Me−N−C catalysts. Fig. 5a displays the LSV curves of P-CoN_4@CNTs, P-NiN_4@CNTs, and P-CuN_4@CNTs, their $E_{1/2}$ values are 0.881, 0.871, and 0.882 V, respectively. Notably, all of these values exceed those of the 20 wt.% Pt/C catalyst. The Tafel slopes of P-CoN_4@CNTs (24.2 mV dec^{-1}), P-NiN_4@CNTs (26.2 mV dec^{-1}), and P-CuN_4@CNTs (29.3 mV dec^{-1}) are calculated. It can be cleared to observe that their Tafel slopes are significantly lower than Pt/C (Fig. S34). Fig. 5b presents the corresponding $E_{1/2}$ and j_K at −0.05 V of different catalysts. As demonstrated in Fig. S35, S36, the electrochemically-active surface areas of different catalysts are evaluated by the double-layer capacitance at the non-Faraday regions. These results collectively affirm the general applicability of the FJH technique for the ultrafast synthesis and activity modulation of atomically-dispersed Me−N−C electrocatalysts.

Given the outstanding oxygen reduction reaction (ORR) performance of the P-FeN_4@CNT catalyst, we utilized it as the air cathode to assemble zinc-air batteries (ZABs) and compared its performance to a control group featuring Pt/C+IrO_2. Remarkably, no significant changes are observed from the galvanostatic discharge curve of the batteries over 12 h at the open-circuit voltages (Fig. 5c). As shown in Fig. 5d, the maximum power density of P-FeN_4@CNT based ZAB reaches 236.3 mW cm^{-2}, significantly higher than that of Pt/C+IrO_2 (118.6 mW cm^{-2}). When increasing the current densities from 1.0 to 200.0 mA cm^{-2}, the P-FeN_4@CNT-based ZAB demonstrates higher discharge voltages (Fig. 5e). Notably, once the current density returned from 200.0 to 1.0 mA cm^{-2}, the voltage plateau stabilized at 1.32 V, closely approaching the initial value of 1.33 V. This behavior underscores the excellent rate performance of the P-FeN_4@CNT-based ZABs. The charge-discharge efficiency and cycle stability of ZABs are evaluated by the long-term charge-discharge tests over 400 h at 5.0 mA cm^{-2} (Fig. 5f). The performances of P-FeN_4@CNT-based ZABs surpass that of the commercial Pt/C+IrO_2 and most Fe−N−C catalysts that have been reported (Table S6). The initial charge-discharge voltage gap of P-FeN_4@CNTs-based ZAB is 0.68 V, lower than that of the Pt/C+IrO_2 (0.78 V). After 400 cycles, only a slight performance loss was observed, with the voltage gap increases by 35 mV. This outcome further highlights the superior durability of the P-FeN_4@CNT catalyst in ZAB applications.

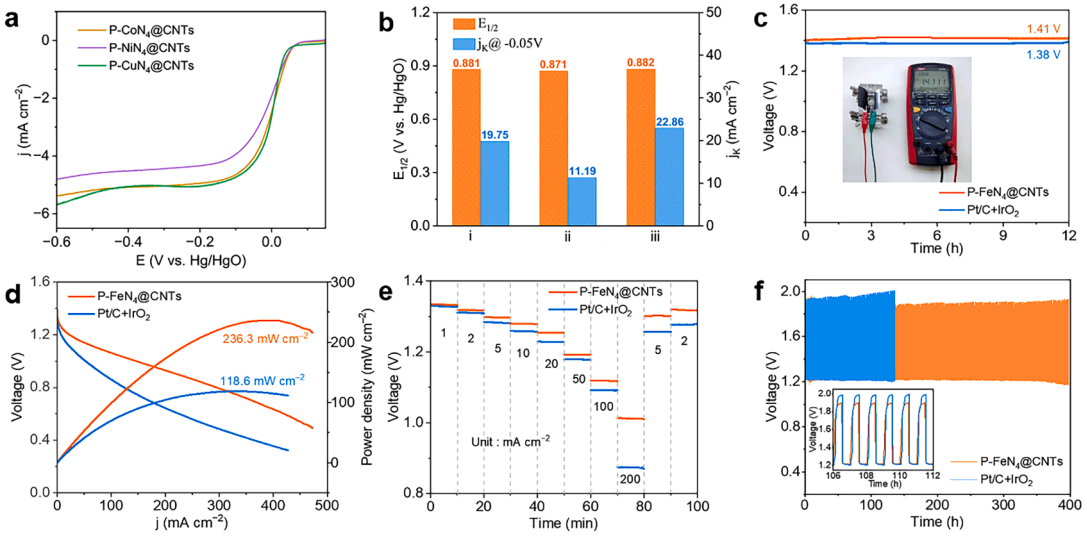

Fig. 5. Performances of the rechargeable zinc-air batteries. (a) ORR LSV curves of P-CoN_4@CNTs, P-NiN_4@CNTs, and P-CuN_4@CNTs catalysts; (b) $E_{1/2}$ and j_K at −0.05 V for P-CoN_4@CNTs (i), P-NiN_4@CNTs (ii), and P-CuN_4@CNTs (iii) catalysts; (c) Open circuit voltages of P-FeN_4@CNTs and Pt/C+IrO_2 based zinc-air batteries; (d) Discharge polarization curves and corresponding power density plots of the Zn-air batteries with P-FeN_4@CNTs and Pt/C+IrO_2 cathodes; (e) Rate performances of P-FeN_4@CNTs and Pt/C+IrO_2 based zinc-air batteries; (f) Charge/discharge cycling curves of P-FeN_4@CNTs and Pt/C+IrO_2 based Zn-air batteries at 5 mA cm^{-2}.

4. Conclusions

In summary, we report the ultrafast and highly efficient synthesis of an atomically-dispersed ORR catalyst of P-FeN_4@CNTs, *via* the FJH technique within 200 milliseconds. This method has been also applied to the preparation of Co, Ni, Cu-based catalysts with desirable catalytic performances, demonstrating the great universality of the FJH strategy for preparing Me–N–C catalysts. Particularly, the optimized P-FeN_4@CNT catalyst exhibits superior electrocatalytic performance, with an $E_{1/2}$ of 0.904 V and a Tafel slope of 23.1 mV dec^{-1}. The introduction of P dopant plays a pivotal role in enhancing the ORR performance. It effectively suppresses N loss during the instantaneous high-temperature FJH process and induces alterations in the local coordination environment of FeN_x centers, leading to uneven charge distribution and a reduced energy barrier for the rate-determining step. As anticipated, the assembled ZAB affords a maximum power density of 236.3 mW cm^{-2}, a low voltage gap of 0.68 V, and excellent cycle stability over 400 h at 5 mA cm^{-2}, while the commercial Pt/C+IrO_2 based battery begins to decay after 100 h. This work highlights the tremendous advantages of FJH technique for the efficient preparation and activity modulation of atomically-dispersed catalysts.

CRediT authorship contribution statement

Guobin Qin: Writing – original draft, Visualization, Investigation, Data curation. **Sida Sun:** Software, Formal analysis. **Xuehuan Zhang:** Visualization, Investigation. **Zhen Han:** Investigation, Formal analysis. **Yanping Li:** Writing – review & editing, Supervision. **Gaoyi Han:** Writing – review & editing, Supervision. **Yan Li:** Writing – review & editing, Supervision. **Sheng Zhu:** Writing – review & editing, Supervision, Resources, Funding acquisition.

Declaration of competing interest

The authors declare that they have no known competing financial interests or personal relationships that could have appeared to influence the work reported in this paper.

Data availability

Data will be made available on request.

Acknowledgements

The work was financially supported by the National Natural Science Foundation of China (22120102004 and U21A6004), Fundamental Research Program of Shanxi Province (202103021223019), Science and Technology Major Project of Shanxi (No. 202101030201022).

Supplementary materials

Supplementary material associated with this article can be found, in the online version, at doi:10.1016/j.ensm.2024.103421.

References

[1] Y. Meng, Y.-M. Zhao, J.-C. Li, C. Shi, L. Zhang, P.-X. Hou, C.H. Liu, M. Cheng, An integrated oxygen electrode derived from a flexible single-walled carbon nanotube film for rechargeable Zn-air batteries produced by electropolymerization, NPG Asia Mater 15 (2023) 14.

[2] H. Li, L. Ma, C. Han, Z. Wang, Z. Liu, Z. Tang, C. Zhi, Advanced rechargeable zinc-based batteries: recent progress and future perspectives, Nano Energy 62 (2019) 550–587.

[3] Q. Huang, X. Zhong, Q. Zhang, X. Wu, M. Jiao, B. Chen, J. Sheng, G. Zhou, Co_3O_4/Mn_3O_4 hybrid catalysts with heterointerfaces as bifunctional catalysts for Zn-air batteries, J. Energy Chem. 68 (2022) 679–687.

[4] Q. Wang, Q. Feng, Y. Lei, S. Tang, L. Xu, Y. Xiong, G. Fang, Y. Wang, P. Yang, J. Liu, W. Liu, X. Xiong, Quasi-solid-state Zn-air batteries with an atomically dispersed cobalt electrocatalyst and organohydrogel electrolyte, Nat. Commun. 13 (2022) 3689.

[5] J. Huang, Y. Zhu, Y. Feng, Y. Han, Z. Gu, R. Liu, D. Yang, K. Chen, X. Zhang, W. Sun, S. Xin, Y. Yu, H. Yu, X. Zhang, L. Yu, H. Wang, X. Liu, Y. Fu, G. Li, X. Wu, C. Ma, F. Wang, L. Chen, G. Zhou, S. Wu, Z. Lu, X. Li, J. Liu, P. Gao, X. Liang, Z. Chang, H. Ye, Y. Li, L. Zhou, Y. You, P. Wang, C. Yang, J. Liu, M. Sun, M. Mao, H. Chen, S. Zhang, G. Huang, D. Yu, J. Xu, S. Xiong, J. Zhang, Y. Wang, Y. Ren, C. Yang, Y. Xu, Y. Chen, Y. Xu, Z. Chen, X. Gao, S.-D. Pu, S. Guo, Q. Li, X. Cao, J. Ming, X. Pi, C. Liang, L. Qie, J. Wang, S. Jiao, Y. Yao, C. Yan, D. Zhou, B. Li, X. Peng, C. Chen, Y. Tang, Q. Zhang, Q. Liu, J. Ren, Y. He, X. Hao, K. Xi, L. Chen, J. Ma, Research progress on key materials and technologies for secondary batteries, Acta Phys. -Chim. Sin. 38 (2022) 2208008.

[6] L. Yang, X. Zhang, L. Yu, J. Hou, Z. Zhou, R. Lv, Atomic Fe–N_4/C in flexible carbon fiber membrane as binder-free air cathode for Zn-air batteries with stable cycling over 1000h, Adv. Mater. 34 (2022) 2105410.

[7] C. Wan, X. Duan, Y. Huang, Molecular design of single-atom catalysts for oxygen reduction reaction, Adv. Energy Mater. 10 (2020) 1903815.

[8] H. Adabi, A. Shakouri, N.U. Hassan, J.R. Varcoe, B. Zulevi, A. Serov, J. R. Regalbuto, W.E. Mustain, High-performing commercial Fe–N–C cathode electrocatalyst for anion-exchange membrane fuel cells, Nat. Energy 6 (2021) 834–843.

[9] L. Dang, H. Liang, J. Zhuo, B.K. Lamb, H. Sheng, Y. Yang, S. Jin, Direct synthesis and anion exchange of non-carbonate-intercalated NiFe layered double hydroxides and the influence on electrocatalysis, Chem. Mater. 30 (2018) 4321–4330.

[10] J. Liu, X. Wan, S. Liu, X. Liu, L. Zheng, R. Yu, J. Shui, Hydrogen passivation of M–N–C (M = Fe, Co) catalysts for storage stability and ORR activity improvements, Adv. Mater. 33 (2021) e2103600.

[11] B. Koyuturk, E.M. Farber, F.E. Wagner, T.-P. Fellinger, D. Eisenberg, A simple decagram-scale synthesis of an atomically dispersed, hierarchically porous Fe–N–C catalyst for acidic ORR, J. Mater. Chem. A 10 (2022) 19859–19867.

[12] A. Zitolo, N. Ranjbar-Sahraie, T. Mineva, J. Li, Q. Jia, S. Stamatin, G.F. Harrington, S.M. Lyth, P. Krtil, S. Mukerjee, E. Fonda, F. Jaouen, Identification of catalytic sites in cobalt-nitrogen-carbon materials for the oxygen reduction reaction, Nat. Commun. 8 (2017) 957.

[13] L. Wei, H. Enis Karahan, S. Zhai, H. Liu, X. Chen, Z. Zhou, Y. Lei, Z. Liu, Yuan. Chen, Amorphous bimetallic oxide-graphene hybrids as bifunctional oxygen electrocatalysts for rechargeable Zn-air batteries, Adv. Mater. 29 (2017) 1701410.

[14] H. Ye, L. Li, D. Liu, Q. Fu, F. Zhang, P. Dai, X. Gu, X. Zhao, Sustained-release method for the directed synthesis of ZIF-derived ultrafine Co–N–C ORR catalysts with embedded Co quantum dots, ACS Appl. Mater. Interfaces 12 (2020) 57847–57858.

[15] M.-Q. Wang, C. Ye, M. Wang, T.-H. Li, Y.-N. Yu, S.-J. Bao, Synthesis of M (Fe_3C, Co, Ni)-porous carbon frameworks as high-efficient ORR catalysts, Energy Storage Mater 11 (2018) 112–117.

[16] L. Jiao, H. Jiang, Metal-organic-framework-based single-atom catalysts for energy applications, Chem 5 (2019) 786–804.

[17] Z. Chen, H. Niu, J. Ding, H. Liu, P.H. Chen, Y.H. Lu, Y.R. Lu, W. Zuo, L. Han, Y. Guo, S.F. Hung, Y. Zhai, Unraveling the origin of sulfur-doped Fe–N–C single-atom catalyst for enhanced oxygen reduction activity: effect of iron spin-state tuning, Angew. Chem. Int. Ed. 60 (2021) 25404–25410.

[18] L. Gong, H. Zhang, Y. Wang, E. Luo, K. Li, L. Gao, Y. Wang, Z. Wu, Z. Jin, J. Ge, Z. Jiang, C. Liu, W. Xing, Bridge bonded oxygen ligands between approximated FeN_4 sites confer catalysts with high ORR performance, Angew. Chem. Int. Ed. 59 (2020) 13923–13928.

[19] Y. He, S. Liu, C. Priest, Q. Shi, G. Wu, Atomically dispersed metal-nitrogen-carbon catalysts for fuel cells: advances in catalyst design, electrode performance, and durability improvement, Chem. Soc. Rev. 49 (2020) 3484–3524.

[20] Y. Zhou, G. Chen, Q. Wang, D. Wang, X. Tao, T. Zhang, X. Feng, K. Müllen, Fe–N–C electrocatalysts with densely accessible Fe–N_4 sites for efficient oxygen reduction reaction, Adv. Funct. Mater. 31 (2021) 2102420.

[21] L. Jiao, J. Li, L.L. Richard, Q. Sun, T. Stracensky, E. Liu, M.T. Sougrati, Z. Zhao, F. Yang, S. Zhong, H. Xu, S. Mukerjee, Y. Huang, D.A. Cullen, J.H. Park, M. Ferrandon, D.J. Myers, F. Jaouen, Q. Jia, Chemical vapour deposition of Fe–N–C oxygen reduction catalysts with full utilization of dense Fe–N_4 sites, Nat. Mater. 20 (2021) 1385–1391.

[22] J. Li, M.T. Sougrati, A. Zitolo, J.M. Ablett, I.C. Oğuz, T. Mineva, I. Matanovic, P. Atanassov, Y. Huang, I. Zenyuk, A. Di Cicco, K. Kumar, L. Dubau, F. Maillard, G. Dražić, F. Jaouen, Identification of durable and non-durable FeN_x sites in Fe–N–C materials for proton exchange membrane fuel cells, Nat. Catal. 4 (2020) 10–19.

[23] X. Huang, T. Shen, T. Zhang, H. Qiu, X. Gu, Zeeshan. Ali, Y. Hou, Efficient oxygen reduction catalysts of porous carbon nanostructures decorated with transition metal species, Adv. Energy Mater. 10 (2020) 1900375.

[24] H. Xu, D. Wang, P. Yang, A. Liu, R. Li, Y. Li, L. Xiao, X. Ren, J. Zhang, M. An, Atomically dispersed M–N–C catalysts for the oxygen reduction reaction, J. Mater. Chem. A 8 (2020) 23187–23201.

[25] H. Shen, L. Yang, Y. Wu, X. Zhang, J. Zhao, Q. Zheng, H. Tang, J. Xie, W. Xu, Influence of activating and supporting oxygen in M–N–C electrocatalysts for oxygen reduction, Electrochim. Acta 466 (2023) 143001.

[26] J. Li, W. Xia, J. Tang, Y. Gao, C. Jiang, Y. Jia, T. Chen, Z. Hou, R. Qi, D. Jiang, T. Asahi, X. Xu, T. Wang, J. He, Y. Yamauchi, Metal-organic framework-derived graphene mesh: a robust scaffold for highly exposed Fe–N_4 active sites toward an excellent oxygen reduction catalyst in acid media, J. Am. Chem. Soc. 144 (2022) 9280–9291.

[27] X. Zhang, G. Han, S. Zhu, Flash nitrogen-doped carbon nanotubes for energy storage and conversion, Small 20 (2024) 2305406.
[28] P. Huang, R. Zhu, X. Zhang, W. Zhang, Effect of free radicals and electric field on preparation of coal pitch-derived graphene using flash Joule heating, Chem. Eng. J. 450 (2022) 137999.
[29] Q. Dong, A.D. Lele, X. Zhao, S. Li, S. Cheng, Y. Wang, M. Cui, M. Guo, A. H. Brozena, Y. Lin, T. Li, L. Xu, A. Qi, I.G. Kevrekidis, J. Mei, X. Pan, D. Liu, Y. Ju, L. Hu, Depolymerization of plastics by means of electrified spatiotemporal heating, Nature 616 (2023) 488–494.
[30] H. Wang, H. Wang, S. Zhang, Y. Zhang, K. Xia, Z. Yin, M. Zhang, X. Liang, H. Lu, S. Li, J. Zhang, Y. Zhang, Carbothermal shock enabled facile and fast growth of carbon nanotubes in a second, Nano Res 15 (2021) 2576–2581.
[31] W. Chen, C. Ge, J.T. Li, J.L. Beckham, Z. Yuan, K.M. Wyss, P.A. Advincula, L. Eddy, C. Kittrell, J. Chen, D.X. Luong, R.A. Carter, J.M. Tour, Heteroatom-doped flash graphene, ACS Nano 16 (2022) 6646–6656.
[32] S. Zhu, F. Zhang, H.-G. Lu, J. Sheng, L. Wang, S.-D. Li, G. Han, Y. Li, Flash nitrogen-doped graphene for high-rate supercapacitors, ACS Mater. Lett. 4 (2022) 1863–1871.
[33] K.M. Wyss, J.T. Li, P.A. Advincula, K.V. Bets, W. Chen, L. Eddy, K.J. Silva, J. L. Beckham, J. Chen, W. Meng, B. Deng, S. Nagarajaiah, B.I. Yakobson, J.M. Tour, Upcycling of waste plastic into hybrid carbon nanomaterials, Adv. Mater. 35 (2023) e2209621.
[34] B. Deng, Z. Wang, W. Chen, J.T. Li, D.X. Luong, R.A. Carter, G. Gao, B.I. Yakobson, Y. Zhao, J.M. Tour, Phase controlled synthesis of transition metal carbide nanocrystals by ultrafast flash Joule heating, Nat. Commun. 13 (2022) 262.
[35] D. Xi, J. Li, J. Low, K. Mao, R. Long, J. Li, Z. Dai, T. Shao, Y. Zhong, Y. Li, Z. Li, X. J. Loh, L. Song, E. Ye, Y. Xiong, Limiting the uncoordinated N species in M–N_x single-atom catalysts toward electrocatalytic CO_2 reduction in broad voltage range, Adv. Mater. 34 (2022) e2104090.
[36] Z.Y. Mei, G. Zhao, C. Xia, S. Cai, Q. Jing, X. Sheng, H. Wang, X. Zou, L. Wang, H. Guo, B. Xia, Regulated high-spin state and constrained charge behavior of active cobalt sites in covalent organic frameworks for promoting electrocatalytic oxygen reduction, Angew. Chem. Int. Ed. 62 (2023) e202303871.
[37] J. Sheng, S. Sun, G. Jia, S. Zhu, Y. Li, Doping effect on mesoporous carbon-supported single-site bifunctional catalyst for Zinc-air batteries, ACS Nano 16 (2022) 15994–16002.
[38] P. Rao, Y. Deng, W. Fan, J. Luo, P. Deng, J. Li, Y. Shen, X. Tian, Movable type printing method to synthesize high-entropy single-atom catalysts, Nat. Commun. 13 (2022) 5071.
[39] L. Li, X. Tang, S. Huang, C. Lu, D. Lutzenkirchen-Hecht, K. Yuan, X. Zhuang, Y. Chen, Longitudinally grafting of graphene with iron phthalocyanine-based porous organic polymer to boost oxygen electroreduction, Angew. Chem. Int. Ed. 62 (2023) e202301642.
[40] J.-W. Huang, Q.-Q. Cheng, Y.-C. Huang, H.-C. Yao, H.-B. Zhu, H. Yang, Highly efficient Fe–N–C electrocatalyst for oxygen reduction derived from core-shell-structured $Fe(OH)_3$@Zeolitic imidazolate framework, ACS Appl. Energy Mater. 2 (2019) 3194–3203.
[41] L. Zheng, S. Yu, X. Lu, W. Fan, C.B. Hi, Y. Ye, X. Shi, J. Zeng, X. Li, S. Liao, Two-dimensional bimetallic Zn/Fe-metal-organic framework (MOF)-derived porous carbon nanosheets with a high density of single/paired Fe atoms as high-performance oxygen reduction catalysts, ACS Appl. Mater. Interfaces 12 (2020) 13878–13887.
[42] F. Xiao, G.-L. Xu, C.-J. Sun, M. Xu, W. Wen, Q. Wang, M. Gu, S. Zhu, Y. Li, Z. Wei, X. Pan, J. Wang, K. Amine, M. Shao, Nitrogen-coordinated single iron atom catalysts derived from metal organic frameworks for oxygen reduction reaction, Nano Energy 61 (2019) 60–68.
[43] J. Zhang, Y. Liu, Z. Yu, M. Huang, C. Wu, C. Jin, L. Guan, Boosting the performance of the Fe–N–C catalyst for the oxygen reduction reaction by introducing single-walled carbon nanohorns as branches on carbon fibers, J. Mater. Chem. A 7 (2019) 23182–23190.
[44] R. Javed, M.A. Khan, D. Ye, Y. Zhao, L.A. Shah, J. Zhang, H. Zhao, Boosting oxygen reduction catalysis through electronic reconfiguration of Fe–N–C induced by P doping, Electrocatalysis 12 (2021) 747–758.
[45] X. Peng, X. Xian, L. Han, Y. Liu, P. Zheng, Y. Fu, P. Dong, X. Zeng, Y. Zhang, Co_2P nanoparticles encapsulated in N-doped carbon nanotubes as a bifunctional oxygen catalyst for a high-performance rechargeable Zn-air battery, ACS Appl. Nano Mater 6 (2023) 2027–2034.
[46] B. Martínez-Sánchez, D. Cazorla-Amorós, E. Morallón, P-functionalized carbon nanotubes promote highly stable electrocatalysts based on Fe-phthalocyanines for oxygen reduction: experimental and computational studies, J. Energy Chem. 72 (2022) 276–290.
[47] J. Guo, X. Yan, Q. Liu, Q. Li, X. Xu, L. Kang, Z. Cao, G. Chai, J. Chen, Y. Wang, J. Yao, The synthesis and synergistic catalysis of iron phthalocyanine and its graphene-based axial complex for enhanced oxygen reduction, Nano Energy 46 (2018) 347–355.
[48] Y. Zhou, R. Lu, X. Tao, Z. Qiu, G. Chen, J. Yang, Y. Zhao, X. Feng, K. Mullen, Boosting oxygen electrocatalytic activity of Fe–N–C catalysts by phosphorus incorporation, J. Am. Chem. Soc. 145 (2023) 3647–3655.
[49] R. Ding, Y. Liu, Z. Rui, J. Li, J. Liu, Z. Zou, Facile grafting strategy synthesis of single-atom electrocatalyst with enhanced ORR performance, Nano Res 13 (2020) 1519–1526.
[50] J. Li, S. Lu, H. Huang, D. Liu, Z. Zhuang, C. Zhong, ZIF-67 as continuous self-sacrifice template derived $NiCo_2O_4$/Co,N–CNTs nanocages as efficient bifunctional electrocatalysts for rechargeable Zn–air batteries, ACS Sust. Chem. Eng. 6 (2018) 10021–10029.
[51] S. Zhu, J. Sheng, G. Jia, Z. Zhang, J. Guo, M. Wang, J. Ni, Y. Li, Monolithic flexible supercapacitors drawn with nitrogen-doped carbon nanotube-graphene ink, Mater. Res. Bull. 139 (2021) 111266.
[52] K. Liu, J. Fu, Y. Lin, T. Luo, G. Ni, H. Li, Z. Lin, M. Liu, Insights into the activity of single-atom Fe–N–C catalysts for oxygen reduction reaction, Nat. Commun. 13 (2022) 2075.
[53] S. Zhu, L. Ding, X. Zhang, K. Wang, X. Wang, F. Yang, G. Han, Biaxially-strained phthalocyanine at polyoxometalate@carbon nanotube heterostructure boosts oxygen reduction catalysis, Angew. Chem. Int. Ed. 62 (2023) e202309545.